PAPER

Check for updates

Formic acid dehydrogenation over PdNi alloys supported on N-doped carbon: synergistic effect of Pd–Ni alloying on hydrogen release†

Rizcky Tamarany,‡[a] Dong Yun Shin,‡[b] Sukho Kang,[b] Hyangsoo Jeong, [iD][a] Joohoon Kim, [iD][cd] Jun Kim, [iD][a] Chang Won Yoon★[ac] and Dong-Hee Lim [iD]★[b]

Bimetallic Pd_1Ni_x alloys supported on nitrogen-doped carbon (Pd_1Ni_x/N−C, x = 0.37, 1.3 and 3.6) exhibit higher activities than Pd/N−C towards dehydrogenation of formic acid (HCO_2H, FA). Density functional theory (DFT) calculations provided electronic and atomic structures, energetics and reaction pathways on Pd(111) and Pd_1Ni_x(111) surfaces of different Pd/Ni compositions. A density of states (DOS) analysis disclosed the electronic interactions between Pd and Ni revealing novel active sites for FA dehydrogenation. Theoretical analysis of FA dehydrogenation on Pd_1Ni_x(111) (x = 0.33, 1 and 3) shows that the Pd_1Ni_1(111) surface provides optimum H_2-release efficiency *via* a favorable 'HCOO pathway', in which a hydrogen atom and one of the two oxygen atoms of FA interact directly with surface Ni atoms producing adsorbed CO_2 and H_2. The enhanced efficiency is also attributed to the blocking of an unfavorable 'COOH pathway' through which a C−O bond is broken and side products of CO and H_2O are generated.

1. Introduction

The development of sustainable energy technology is currently one of the most urgent and important challenges in mitigating global energy and environmental issues related to climate change.[1–4] A universal transition to renewable energy is required to provide sustainable resources in future societies. To efficiently utilize renewable energy produced in an intermittent and unpredictable manner, a carbon-free and high-capacity energy carrier is needed. In the regard, hydrogen (H_2) has long been recognized as a viable and consistent energy carrier owing to its high gravimetric energy density (*ca.* 33.3 kW h kg^{-1}-H_2).[5] In addition, use of hydrogen in a fuel cell that produces electricity and water as the only byproducts is effective in many portable, stationary and transportation applications.[6–10] However, because gaseous hydrogen has a very low volumetric energy density, current pressurized storage technologies (*e.g.*, 700 bar H_2, 40 g H_2 per L)[11] may not meet the geographical and temporal gaps between the hydrogen supply and demand site. For this reason, hydrogen storage in liquid chemicals has received particular attention for high-capacity storage and long-distance transport because liquid hydrogen carriers allow to store large amounts of hydrogen and to affordably deliver it to desired sites using the currently existing infrastructure.[5,9,10,12,13]

A promising candidate for liquid-based hydrogen storage materials is formic acid (HCO_2H, FA). Formic acid is a relatively nontoxic liquid with a large volumetric hydrogen storage density (53 g L^{-1}), which allows it to be economically stored and transported. The hydrogen atoms of FA can be liberated with an appropriate catalyst under ambient conditions ($HCO_2H \rightarrow H_2 + CO_2$). Moreover, FA can also be produced by biomass processing[6,14–19] and catalytically or electrocatalytically generated by hydrogenation of carbon dioxide ($H_2 + CO_2 \rightarrow HCO_2H$) using excess renewable energy.[16,18,20] These properties make FA appealing as a hydrogen carrier applicable to decentralized fuel cell power generation, hydrogen refueling stations and large-scale renewable energy storage systems.[21]

A highly efficient catalyst is needed to release hydrogen from FA in a controllable manner and to facilitate its application in various energy-requiring scenarios. Successful heterogeneous catalysts were developed to selectively catalyze FA dehydrogenation include numerous Pd-based nanomaterials: Pd nanoparticles (NPs),[15–17,19,22–24] PdM (M = Ag, Au, Ni, Co) core–shells[25–30]

[a] *Center for Hydrogen and Fuel Cell Research, Korea Institute of Science and Technology (KIST), 5 Hwarang-ro 14-gil, Seongbuk-gu, Seoul 02792, Republic of Korea. E-mail: cwyoon@kist.re.kr*

[b] *Department of Environmental Engineering, Chungbuk National University, Chungdae-ro 1, Seowon-gu, Cheongju, Chungbuk 28644, Republic of Korea. E-mail: limkr@cbnu.ac.kr*

[c] *KHU-KIST Department of Converging Science and Technology, Kyung Hee University, 26 Kyungheedae-ro, Dongdaemun-gu, Seoul 02447, Republic of Korea*

[d] *Department of Chemistry, Research Institute for Basic Sciences, Kyung Hee University, 26 Kyungheedae-ro, Dongdaemun-gu, Seoul 02447, Republic of Korea*

† Electronic supplementary information (ESI) available. See DOI: 10.1039/d1cp00236h

‡ First authors equally contributed to this work.

This journal is © the Owner Societies 2021

Phys. Chem. Chem. Phys., 2021, **23**, 11515–11527 | **11515**

and Pd-based alloys.[25,27,29,31–35] The superior performance of these catalysts is thought to originate from electronic structural modifications that create active sites by alloying with a different metal[27,32–34] and/or by using supports with nitrogen dopants or nitrogen-containing (amine) functionalities.[16,17,19,28] Pd-Based alloy catalysts without other noble metals also have been reported to reduce the cost of catalyst implementation. For example, a PdNi@Pd catalyst exhibits good FA dehydrogenation activity at room temperature.[29] Pd–Co-based nanoparticles are multifunctional catalysts for FA dehydrogenation and methanol oxidation.[30] A boron-doped Pd catalyst displays greater activity than bimetallic Pd–Au catalysts for hydrogen generation from aqueous formic acid/formate solutions at room temperature.[15] However, a remaining challenge is to develop relatively inexpensive catalysts that can rapidly produce hydrogen by dehydrogenation. Increased temperature can improve the rate of H_2-release from FA, but the accompanying dehydration reaction ($HCO_2H \rightarrow H_2O + CO$) could also take place to produce carbon monoxide which deactivates the Pt catalysts in polymer electrolyte membrane fuel cells (PEMFCs). Therefore, understanding the pathways of FA dehydrogenation over low-cost, bimetallic Pd-based materials is of significant importance in gaining insight to the development of highly active and selective heterogeneous catalysts.

In this paper, we report experimental and theoretical studies of FA dehydrogenation over Pd_1Ni_x alloy catalysts ($x = 0.37, 1.3$ and 3.6) supported on nitrogen-doped carbon (Pd_1Ni_x/N–C) as model Pd based alloy catalysts possessing an inexpensive transition metal. The nanostructured PdNi active sites prepared by a simple wet chemical method are characterized by a number of different analytical techniques. The PdNi/N–C catalysts exhibit greater FA dehydrogenation activity than a Pd/N–C catalyst. The electronic structure of the PdNi alloys and the FA decomposition mechanisms are elucidated using density functional theory (DFT) calculations. The results demonstrate the cooperative role of the Pd–Ni active sites in rotating a key HCOO intermediate as well as in activating the C–H bonds of FA during dehydrogenation. In addition, the $Pd_1Ni_{1.3}$ active sites prove to prevent a H_2O and CO formation step (dehydration) over the H_2 and CO_2 formation step (dehydrogenation).

2. Experimental and computational methodology

2.1. Synthesis of nitrogen-doped carbon support (N–C) and Pd/N–C, PdNi/N–C and Ni/N–C catalysts

Palladium(II) nitrate dihydrate [$Pd(NO_3)_2·2H_2O$], nickel(II) nitrate hexahydrate [$Ni(NO_3)_2·6H_2O$] and dicyandiamide [$NH_2C(=NH)NHCN$] were purchased from Sigma-Aldrich. Dicyandiamide was used to prepare a nitrogen doping precursor. Carbon black (Ketjen) was purchased from Akzo Nobel. Unless noted, other chemicals were used without further purification.

For the materials synthesis, the nitrogen-doped carbon support was initially prepared by adding dicyandiamide

(1.0 g, 12 mmol) to an aqueous solution (50 mL) containing carbon black (1.0 g) followed by heating at 100 °C for 4 h with vigorous stirring to vaporize the water. Black solids were obtained upon complete drying. The resulting solids were ground and pyrolyzed at 550 °C for 4 h under a N_2 flow yielding the final N–C products as black powders. The N–C support was characterized using XRD.

Pd_1Ni_x alloys supported on N–C (Pd_1Ni_x/N–C) were prepared by dispersing N–C into aqueous solutions containing $Pd(NO_3)_2·2H_2O$ and $Ni(NO_3)_2·6H_2O$ at different Pd/Ni mole ratios (1/0.33, 1/1 and 1/3). The distilled water in the heterogeneous mixture was evaporated slowly by stirring. The resulting black powders were collected and reduced under a H_2/N_2 flow (20% H_2) at 450 °C for 4 h, affording Pd_1Ni_x/N–C. The Pd_1Ni_x nanoparticles on the N–C supports were determined to have Pd/Ni mole ratios of $Pd_1Ni_{0.37}$, $Pd_1Ni_{1.3}$, $Pd_1Ni_{3.6}$, respectively, by ICP-OES (ESI,† Section S1 and Table S1). Pd/N–C and Ni/N–C materials were synthesized for comparison using solely $Pd(NO_3)_2·2H_2O$ and $Ni(NO_3)_2·6H_2O$, respectively, by the Pd_1Ni_x/N–C procedure. $Pd_1Ni_{1.3}$/C also was prepared by the above procedure using a commercial carbon support (Ketjen). The Pd/Ni ratio in $Pd_1Ni_{1.3}$/C was determined using TEM-EDS.

2.2. Characterization

Inductively coupled plasma-optical emission spectroscopy (ICP-OES) was used to analyze the chemical composition of the PdNi nanoparticles (NPs). Measurements were performed on an ICP-OES Varian 720ES Agilent instrument using a cross-flow nebulizer with the following parameters: plasma, 18.0 L Ar per min; auxiliary, 0.3 L Ar per min; nebulizer, 0.73 L Ar per min; power, 1500 W; peristaltic pump rate, 1.40 mL min^{-1}.

High-angle annular dark-field scanning transmission electron microscopy (HAADF-STEM) was used to determine the morphology of the catalysts. Elemental distributions in PdNi NPs were obtained by energy dispersive X-ray spectroscopy (EDS). Samples were prepared by drop-casting an ethyl alcohol suspension of carbon-supported NPs onto a carbon-coated Cu grid followed by solvent evaporation at room temperature. Measurements were performed on an FEI Talos G_2 80–200 Chemi-STEM electron microscope at 200 kV.

X-Ray photoelectron spectroscopy (XPS) analysis was conducted *ex situ* using a PHI 5000 Versa Probe (Ulvac-PHI). The system used a focused monochromatic Al Kα (1486.6 eV) source for excitation and a spherical section analyzer. The 100 W, 100 μm diameter X-ray beam was rastered over a 1.4 mm × 0.2 mm rectangular spot on the sample. The beam was incident to the sample normally, and the detector was placed at 45° from the normal. The binding energy (BE) scale was calibrated using the C 1s peak (284.6 eV) as an internal standard. XRD measurements were performed using Cu Kα radiation ($λ = 0.154$ nm) at the 11-ID-C beamline with a Rigaku Miniflex II X-ray diffractometer. For *ex situ* experiments, PdNi/N–C samples were loaded into thin glass capillaries open at one end. The scan rate was set at 4°/min with a scan range of $10° \leq 2θ \leq 90°$. Crystallite sizes of Pd_1Ni_x/N–C ($x = 0, 0.37, 1.3$ and 3.6) and Ni/N–C were calculated using the Scherrer method, and summarized

11516 | *Phys. Chem. Chem. Phys.*, 2021, **23**, 11515–11527

This journal is © the Owner Societies 2021

in Table S2 (ESI†). In addition, XPS Pd_{3d} data for Pd_1Ni_x/N–C (x = 0, 0.37, 1.3 and 3.6) were analyzed and relevant peak positions were listed in Table S3 (ESI†).

2.3. Catalytic activity measurements

Catalytic reactions were performed at a desired temperature of 30 °C in a two-neck glass tube. One neck of the reactor was connected to an Ar gas supply. The other was connected to a gas burette to determine the quantity of gas released in real time. The gas burette is filled with oil to prevent potential CO_2 dissolution in water. The reaction tube was cleaned with Ar gas prior to reaction. Catalytic FA dehydrogenation was initiated by introducing a 10 mL mixture of FA (HCO_2H, 1.0 M) and sodium formate (HCO_2Na, 1.0 M) to the reaction tube containing a desired catalyst followed by stirring under ambient conditions. The Pd quantities in a series of Pd_1Ni_x (x = 0, 0.37, 1.3 and 3.6) supported on nitrogen-doped carbon were listed as follows: Pd/N–C, n_{Pd} = 12.7 µmol; $Pd_1Ni_{0.37}$/N–C, n_{Pd} = 12.5 µmol and n_{Ni} = 4.61 µmol; $Pd_1Ni_{1.3}$/N–C, n_{Pd} = 12.2 µmol and n_{Ni} = 15.9 µmol; $Pd_1Ni_{3.6}$/N–C, n_{Pd} = 11.6 µmol and n_{Ni} = 41.7 µmol. The volume of gas produced was determined using an automatic gas burette system directly connected to the reactor for real-time volumetric measurements. In a separate experiment, the influence of temperature on FA dehydrogenation over $Pd_1Ni_{1.3}$/N–C and Pd/N–C was monitored by varying reaction temperatures (25 °C, 45 °C and 65 °C) using the identical quantities of HCO_2H and $NaHCO_2$. The $Pd_1Ni_{1.3}$/N–C material was prepared at a fixed Pd content (n_{Pd}) of 8.9 µmol, followed by testing the temperature-dependent FA dehydrogenation. Unless otherwise noted, initial TOFs were calculated using the total amount of gas produced at 5 min by the following equation (eqn (1) and (2)). TOF values for FA dehydrogenation over Pd_1Ni_x/N–C (x = 0, 0.37, 1.3 and 3.6) obtained at different temperatures were listed in Table S4 (ESI†). Further, the catalytic activities of the as-prepared catalysts toward formic acid decomposition were compared to those of other Pd based bi- and trimetallic catalysts reported previously (Table S5, ESI†).

$$\text{moles of } H_2 \text{(in 5 min)}, \quad n_{H_2} = \frac{P_{atm}\left(\dfrac{V_{gas}}{2}\right)}{RT} \quad (1)$$

$$\text{TOF } (h^{-1}) = \frac{\text{moles of } H_2, n_{H_2}}{\text{moles of Pd used} \times \text{time}} \quad (2)$$

2.4. Computational methodology

Plane-wave periodic DFT calculations were performed using the Vienna *ab initio* simulation package (VASP).[36–38] The projector-augmented wave (PAW)[39,40] was used to describe electron–ion interactions. The exchange–correlation function was described by PW91-GGA with spin polarization.[41,42] The Kohn–Sham one-electron states were expanded into a plane-wave basis set up with a 400 eV cut-off energy. Brillouin zone sampling was employed using a Monkhorst–Pack grid.[43] The k-point samplings were set at $16 \times 16 \times 16$ and $4 \times 4 \times 1$ for bulk

and surface calculations, respectively. Methfessel–Paxton smearing with a value of 0.1 eV was applied.[44]

The energy of gas-phase molecules was calculated using a single molecule in a 12 Å cube with gamma-point sampling. The metal (111) surfaces were modeled by a periodic slab containing four atomic layers with full relaxation of the uppermost two layers. A $p(4 \times 4)$ super cell with an 18 Å vacuum space in the z direction was used for the surface (111) slab models to prevent interaction with periodic images. The result of surface coverage is shown in Table S6 (ESI†).

The nudged elastic band (NEB) method was used to find a minimum energy path between the initial and final states where both states are local minima on the potential energy surface.[45,46] In this approach, the reaction path was discretized with the distinct configurations or images between the energy minima connected by elastic springs to prevent the images from sliding to the minima during optimization. Convergence criteria for electronic and atomic relaxations were set at 10^{-4} and 10^{-2} eV, respectively. The k-points were selected as $2 \times 2 \times 1$ to optimize computing time and performance. To verify the use of the smaller number of k-points for the activation energy calculations, the NEB calculations were conducted by using k-points of $4 \times 4 \times 1$ for a key step of the reactions on both Pd(111) and Pd_1Ni_1(111). There was little difference in the activation energies (difference smaller than 0.02 eV), indicating that k-points grids of $2 \times 2 \times 1$ would not affect the accuracy of activation energy. The calculated activation energies for a key step are shown in Table S7 (ESI†).

Bader charge calculations[47,48] were conducted for the most stable models of Pd(111), $Pd_1Ni_{0.33}$(111), Pd_1Ni_1(111) and Pd_1Ni_3(111) surfaces containing an adsorbed H atom. The electron charge transfer between adsorbate and surface was determined by subtracting the Bader charge of the free adsorbate plus clean surface from that of surfaces containing adsorbates to obtain the excess Bader charge. Positive and negative excess Bader charge values represent the gain and loss of charge, respectively, upon adsorption to the catalytic surfaces.

3. Results and discussion

3.1. Synthesis and characterization of Pd_1Ni_x materials

The bulk compositions of the Pd_1Ni_x/N–C catalysts determined by ICP-OES are represented in terms of mole ratios as $Pd_1Ni_{0.37}$, $Pd_1Ni_{1.3}$ and $Pd_1Ni_{3.6}$ (Table S1, ESI†). The structures of the bimetallic Pd_1Ni_x/N–C alloy materials (x = 0.37, 1.3 and 3.6) were first verified by HAADF-STEM and XRD analyses. Representative HAADF-STEM images indicate that $Pd_1Ni_{1.3}$/N–C has a smaller average PdNi NP size (3.1 nm) with higher particle dispersion compared to $Pd_1Ni_{1.3}$/C (7.9 nm) suggesting that the N-doped carbon support helps form relatively small PdNi NPs in a well-dispersed manner (Fig. 1). $Pd_1Ni_{0.37}$/N–C and $Pd_1Ni_{3.6}$/N–C likewise exhibit smaller average metallic sizes of 3.0 and 2.5 nm, respectively (Fig. S1, ESI†). This result is consistent with previous reports that Pd supported on mesoporous graphitic carbon nitride (mpg-C_3N_4)[16] or N-doped
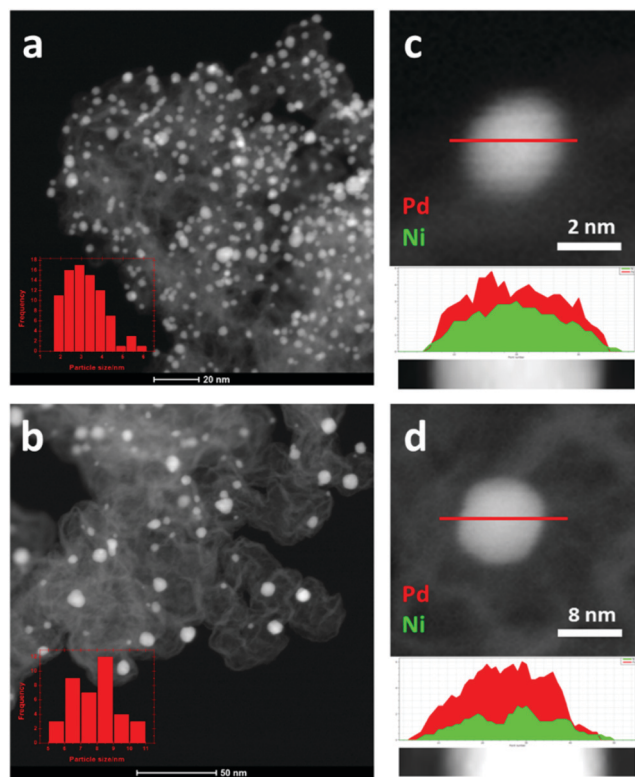
This journal is © the Owner Societies 2021

Phys. Chem. Chem. Phys., 2021, **23**, 11515–11527 | **11517**

Fig. 1 HAADF-STEM images of (a) $Pd_1Ni_{1.3}$/N–C and (b) $Pd_1Ni_{1.3}$/C and line profiles for (c) $Pd_1Ni_{1.3}$/N–C and (d) $Pd_1Ni_{1.3}$/C.

carbon provides better Pd dispersion than Pd/C. The line profiles of $Pd_1Ni_{1.3}$ supported on C and N–C indicate formation of PdNi alloys over the entire surfaces (Fig. 1c and d). Elemental mapping of $Pd_1Ni_{1.3}$/N–C by HAADF-STEM confirms overlap of the Pd and Ni positions consistent with the formation of PdNi alloys (Fig. S2, ESI†).

The structure of the Pd_1Ni_x/N–C (x = 0, 0.37, 1.3 and 3.6) alloys was further confirmed by XRD analysis. Fig. 2a shows XRD patterns of Pd_1Ni_x/N–C as a function of the Pd/Ni ratio. The diffraction peak centered at 39.1° corresponding to the crystalline Pd nanoparticles in Pd/N–C shifts to larger diffraction angles as the Ni content increases. This indicates a gradual decrease in lattice constants due to incorporation of the smaller Ni atoms into the Pd lattice upon forming the Pd_1Ni_x alloys: Pd, 39.1°; $Pd_1Ni_{0.37}$, 39.4°; $Pd_1Ni_{1.3}$, 39.9°; and $Pd_1Ni_{3.6}$, 40.0°. It has been reported that Pd and Ni form an isomorphous alloy with a face-centered cubic (fcc) structure over the entire composition range.[49,50] Crystallite sizes calculated using the Scherrer method and based on the XRD results (Table S2, ESI†) exhibit similar particle sizes close to those observed by TEM. The electronic (Pd 3d) states of the alloyed catalysts were further characterized by XPS. Fig. 2b shows that the $Pd(3d_{5/2})$ and $Pd(3d_{3/2})$ binding energies in Pd_1Ni_x/N–C (x = 0, 0.37, 1.3 and 3.6) increase slightly relative to those of Pd/N–C with increasing Ni content. In the XPS spectra, the peaks were further deconvoluted to give two separable peaks attributed to Pd^0 (blue peaks) and Pd^{2+} (green peaks) species, respectively, presenting increased binding energies as Ni content increased. The binding energies (eV) as a
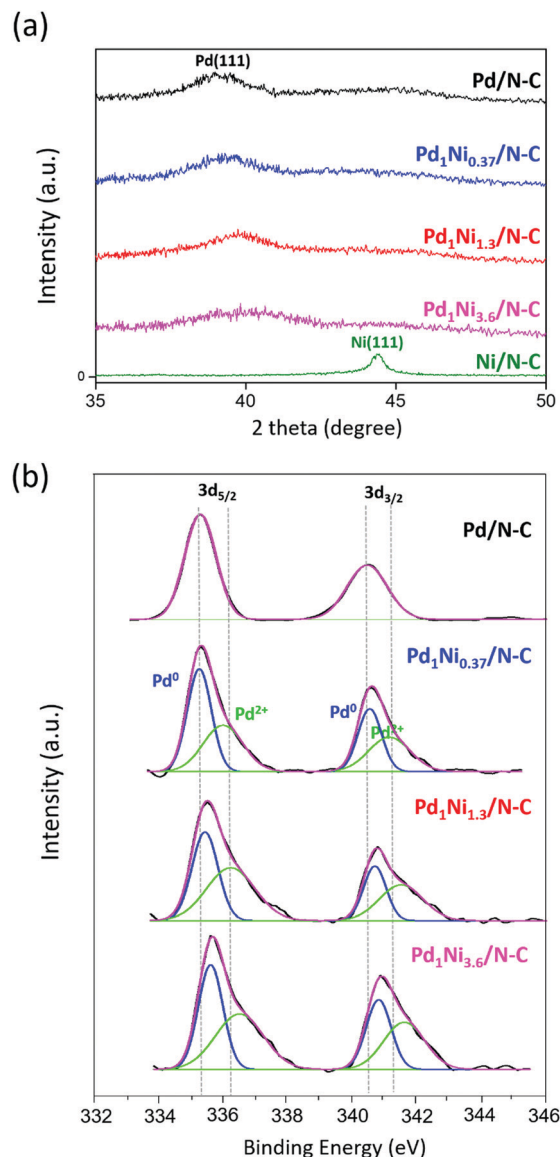

Fig. 2 (a) XRD analyses of Pd_1Ni_x/N–C (x = 0, 0.37, 1.3 and 3.6) and (b) XPS Pd 3d spectra of Pd_1Ni_x/N–C (x = 0, 0.37, 1.3 and 3.6). The blue and green curves represent deconvoluted peaks attributed to Pd^0 and Pd^{2+}, respectively.

function of composition are summarized in ESI† (Table S3). These results are consistent with increases in the Pd 3d XPS binding energies of Pd_1Ni_x alloys (x = 0.33, 1 and 3) employed for CO oxidation[51] and further indicate the presence of electronic interactions between Pd and Ni in the PdNi alloys.

3.2. Catalytic activity towards FA dehydrogenation over Pd_1Ni_x (x = 0, 0.37, 1.3 and 3.6)

Five materials (Pd/N–C, $Pd_1Ni_{0.37}$/N–C, $Pd_1Ni_{1.3}$/N–C, $Pd_1Ni_{3.6}$/N–C and Ni/N–C) were employed to initially examine the influence of Pd/Ni ratio on H_2-release rate from aqueous 1.0 M HCO_2H plus 1.0 M sodium formate as a Brønsted base at 30 °C. Fig. 3a shows that Ni/N–C exhibits negligible FA dehydrogenation activity, whereas Pd/N–C displays much

11518 | Phys. Chem. Chem. Phys., 2021, 23, 11515–11527

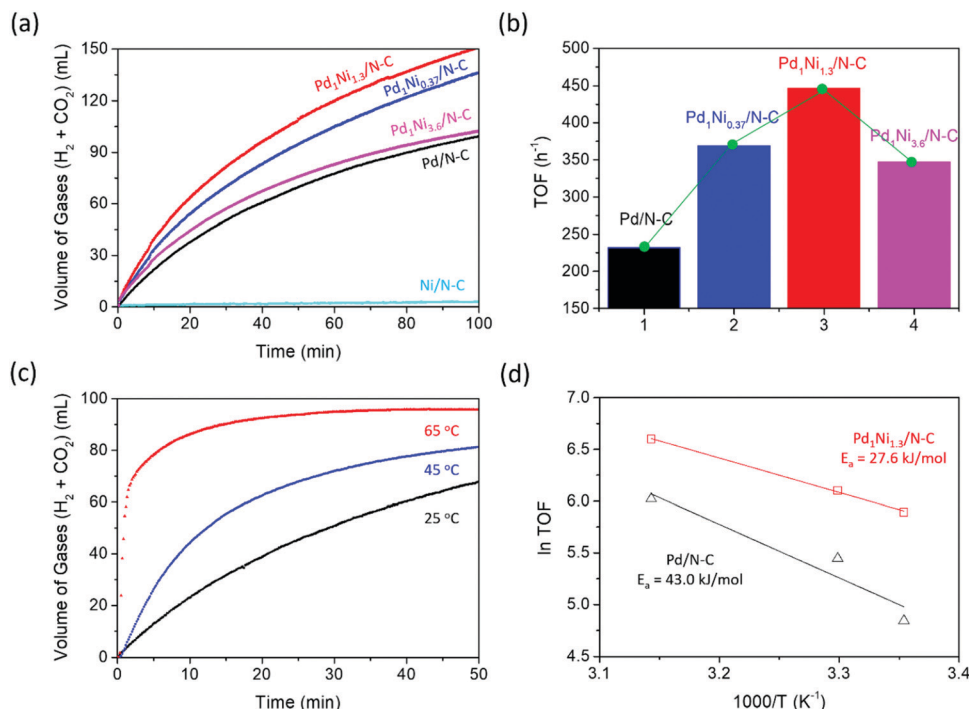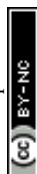This journal is © the Owner Societies 2021

Fig. 3 (a) Gas (H_2 + CO_2) evolution profiles from 10 mL of aqueous FA/formate (1.0 M HCO_2H, 1.0 M HCO_2Na) solution with Pd-based catalysts (Pd, 11.6–12.7 µmol) at 30 °C. (b) TOFs obtained using Pd_1Ni_x/N–C (x = 0, 0.37, 1.3 and 3.6) (c) temperature dependent gas (H_2 + CO_2) evolution obtained using $Pd_1Ni_{1.3}$/N–C (Pd, 8.9 µmol). (d) Arrhenius plots based on initial rates at 25, 30 and 45 °C. Hollow squares and triangles represent $Pd_1Ni_{1.3}$/N–C and Pd/N–C, respectively.

higher activity with *ca.* 100 mL of gases (H_2 + CO_2) being released within 100 min of reaction time. Upon utilization of Pd_1Ni_x/N–C (x = 0.37, 1.3 and 3.6), their catalytic activities were further increased compared to that of Pd/N–C. In addition, the catalysts with three different Pd/Ni ratios showed volcano-type behavior where the highest activity was obtained over $Pd_1Ni_{1.3}$/N–C (Fig. 3b). These results emphasize the important role of Ni in perturbing the Pd electronic structure, thereby facilitating H_2-release from aqueous FA solution. In line with the results, XPS analysis (Fig. 2b) also suggests constructive interaction between Pd and Ni atoms possibly leading to the formation of new active sites responsible for the enhanced FA dehydrogenation activity. To determine composition of the released gases during formic acid decomposition, separate experiments were carried out using newly prepared Pd_1Ni_x catalysts (x = 0.37, 1.3 and 3.6). Analysis with gas chromatography (GC) revealed the formation of H_2 and CO_2, with no CO gas being formed (Fig. S3, ESI†). The calculated turnover frequencies (TOFs) for $Pd_1Ni_{0.37}$/N–C, $Pd_1Ni_{1.3}$/N–C and $Pd_1Ni_{3.6}$/N–C of 369, 447 and 347 h^{-1}, respectively, at 30 °C are greater than that of Pd/N–C (TOF = 232 h^{-1} at 30 °C) under identical reaction conditions (Table S4, ESI†). Likewise, the TOF of $Pd_1Ni_{1.3}$/C (TOF = 363 h^{-1}) determined at 25 °C is much higher than those of Pd/N–C (TOF = 127 h^{-1}), $Pd_1Ni_{1.3}$/C (TOF = 85.5 h^{-1}) and Pd/C (TOF = 37.5 h^{-1}) obtained at 25 °C.

In a separate experiment, the influence of temperature on dehydrogenation activity was studied using $Pd_1Ni_{1.3}$/N–C as a function of temperature (Fig. 3c). TOFs of 363, 736 and

2195 h^{-1} were obtained using the initial 5 min data at 25, 45 and 65 °C, respectively. It is noted that the TOF of 2195 h^{-1} at 65 °C was underestimated because the rate of H_2-release based on the initial 5 min data was estimated using both linear and curved sections; when considering the initial 2 min data for dehydrogenation, the TOF at 65 °C increases to 4804 h^{-1}. Given that the added Brønsted base, sodium formate can potentially react with water to release hydrogen (HCO_2Na + H_2O → HCO_3Na + H_2) particularly at temperatures of >65 °C in the presence of a Pd based catalyst,[21] the observed rapid H_2-release at 65 °C not only originates from FA decomposition (HCO_2H → CO_2 + H_2), but it could also come from formate dehydrogenation (HCO_2^- + H_2O → HCO_3^- + H_2). To avoid the potential formate dehydrogenation effect, Arrhenius plots were obtained based on the TOFs determined at the low temperatures of 25, 30 and 45 °C. The activation energies calculated from the temperature dependent rate of FA dehydrogenation (Fig. 3d) were 27.6 and 43.0 kJ mol^{-1} for $Pd_1Ni_{1.3}$/N–C and Pd/N–C, respectively. The results again support the positive effect of PdNi alloying on H_2-release from FA. The apparent prefactor, A values were then calculated using the Arrhenius equation, presenting 2.5×10^7 s^{-1} and 4.9×10^9 s^{-1} for $Pd_1Ni_{1.3}$/N–C and Pd/N–C, respectively. Since pre-exponential factor is related to the amount of times molecules hit in the orientation necessary to cause a reaction, this collision factor is higher in Pd/N–C catalyst than that of $Pd_1Ni_{1.3}$/N–C catalyst although the activation energy value itself is lower for $Pd_1Ni_{1.3}$/N–C catalyst (27.6 kJ mol^{-1}) than that of Pd/N–C catalyst (43.0 kJ mol^{-1}).

This journal is © the Owner Societies 2021

Phys. Chem. Chem. Phys., 2021, **23**, 11515–11527 | **11519**

Pd-Based bimetallic catalysts for FA decomposition have been developed to reduce Pd contents and the effect of Pd–M alloys (M = transition metals) on FA dehydrogenation has been studied. For instance, comparing dehydrogenation catalysts utilizing carbon-based supports, $Pd_{59}Au_{41}$/C[32] and $Pd_{25}Au_{75}$/C[52] were reported to liberate molecular hydrogen from FA with the TOFs of 230 h^{-1} (at 50 °C) and 212 h^{-1} (at 75 °C), respectively. Similarly, monodispersed $Ag_{42}Pd_{58}$[53] alloy nanoparticles were also found to be active and durable catalysts for FA decomposition at 50 °C, with the TOF of 382 h^{-1}. In addition to numerous PdAu and PdAg catalysts, Pd-based bimetallic catalysts alloyed with non-precious metals were also developed. A PdNi@Pd/GNs–CB[29] (GNs–CB = graphene nanosheets–carbon black) catalyst was synthesized and tested for FA dehydrogenation at room temperature, presenting a high activity with the TOF of 577 h^{-1} calculated based on the number of active sites determined. Compared to the PdNi/GNs–CB catalyst, the as-developed Pd_1Ni_x/N–C (x = 0.37, 1.3 and 3.6) material exhibits comparable TOFs at the similar temperature of 30 °C. Compared to catalysts possessing precious metals, our catalysts could likely be economically advantageous. Additionally, the nitrogen-doped carbon support employed in the Pd_1Ni_x/N–C catalysts can readily be mass produced. In addition to the beneficial effect of PdNi alloys on FA dehydrogenation, nitrogen-doped carbon employed can also provide a positive effect in increasing catalytic activity by donating charge density to the PdNi sites. Catalytic activities of Pd-based bi- and tri-metallic catalysts for formic acid dehydrogenation were compared (Table S5, ESI†). To elucidate how Ni alloying affects the reactivity on FA decomposition, mechanistic pathways were further explored by theory with relevant energetic consideration.

3.3. Possible mechanism of FA dehydrogenation

3.3.1. Bulk and surface models of Pd_1Ni_x alloys. DFT calculations were conducted to investigate the pathways of FA dehydrogenation by constructing $Pd_1Ni_{0.33}$, Pd_1Ni_1 and Pd_1Ni_3

model systems corresponding, respectively, to the experimental $Pd_1Ni_{0.37}$, $Pd_1Ni_{1.3}$ and $Pd_1Ni_{3.6}$ catalysts. The bulk structures were designed considering the atomic arrangement used for simulating bimetallic alloys in DFT calculations.[54–56] The calculated lattice parameter of bulk fcc-Pd was 3.95 Å, which is close to the experimental value of 3.89 Å.[57] The *fcc* lattice parameters of bulk $Pd_1Ni_{0.33}$ and Pd_1Ni_3 calculated in an identical manner were 3.87 Å and 3.65 Å (a = b = c). However, the *fcc* crystal structure obtained for Pd_1Ni_1 was shrunken unevenly from that of bulk *fcc*-Pd with values of 3.85 and 3.59 Å for lattice parameters a = b and c, respectively (Fig. S4, ESI†). The decrease in Pd lattice parameters comes from the incorporation of smaller Ni atoms consistent with the observation that the diffraction peak corresponding to the Pd(111) plane shifts to larger angles in the XRD analysis (Fig. 2a). The HCOOH bond lengths obtained from free gas-phase calculations were 0.984 (O–H), 1.104 (C–H), 1.210 (C=O) and 1.353 (C–O) Å (Table S8, ESI†) in agreement with experimental values of 0.972 (O–H), 1.097 (C–H), 1.202 (C=O) and 1.343 (C–O) Å, respectively.[58]

3.3.2. Electronic structures of Pd(111) and PdNi(111). The relative location of the d-band center of an active site is useful in predicting the activity of FA dehydrogenation catalysts. The d-band centers of Pd_1Ni_x prepared by alloying a pure Pd surface are likely shifted closer to the Fermi level. The electronic perturbation induced by Ni alloying may increase the inter-action between active sites and adsorbates, which will further increase the catalytic activity for FA dehydrogenation. Thus, the d-band centers of neighboring Pd–Pd and Pd–Ni atoms on Pd(111) and Pd_1Ni_x(111) surfaces were calculated as a function of composition.

Fig. 4 shows that the d-band centers of Pd–Pd shift to more negative values with increasing Ni content implying that the metal–adsorbate interaction decreases as: Pd(111) > $Pd_1Ni_{0.33}$(111) > Pd_1Ni_1(111) > Pd_1Ni_3(111). However, the d-band centers of Pd–Ni shift to more positive values or closer
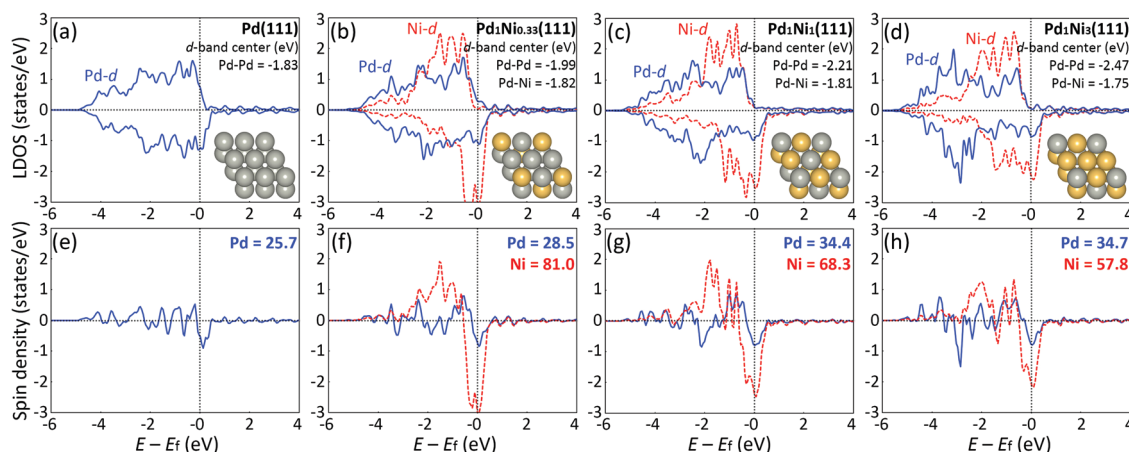
Fig. 4 The d-band structures and center values of neighboring Pd and Ni atoms represented by the local density of states (LDOS) for: (a) Pd(111), (b) $Pd_1Ni_{0.33}$(111), (c) Pd_1Ni_1(111) and (d) Pd_1Ni_3(111) surfaces. The grey and yellow spheres represent Pd and Ni atoms, respectively. The spin density (the sum of absolute value of difference between the electron densities of the spin-up and spin-down electrons) of individual Pd and Ni atoms in each system is shown in the second row of panels (e–h).

11520 | *Phys. Chem. Chem. Phys.*, 2021, **23**, 11515–11527

This journal is © the Owner Societies 2021

to the Fermi level potentially leading to enhanced interaction between metal atoms and adsorbates. Considering that catalytic activity is high when the strength of substrate adsorption is moderate, the d-band centers that decrease (in the Pd–Pd case) and increase (in the Pd–Ni case) with increasing Ni mole fraction suggest that there is a balance point at which an appropriate Ni content maximizes activity. The changes in spin density of individual Pd and Ni atoms in the Pd–Ni alloys are inversely proportional to one another upon changing the Ni content. Previous studies reported that asymmetric spin density showed high catalytic activity for oxygen reduction reaction (ORR) and $HCOO^-$ dehydrogenation by improving the adsorption of intermediates.[59,60] Thus, greater spin density, which is the difference between the electron densities of the spin-up and spin-down electrons, may correlate with higher catalytic activity. This result supports the existence of a balance point where there is optimum catalytic activity of the Pd_1Ni_1 alloy. The $Pd_1Ni_1(111)$ surface also provides more Pd–Ni interactions compared to the $Pd_1Ni_{0.33}(111)$ and $Pd_1Ni_3(111)$ surfaces (Fig. 4b–d, insets). The effect of spin density on adsorption is discussed in ESI,† Section S2.

Fig. 4d also shows that the degree of d-orbital hybridization of Pd and Ni on the $Pd_1Ni_3(111)$ surface is somewhat lower than on the $Pd_1Ni_{0.33}(111)$ and $Pd_1Ni_1(111)$ surfaces. The degree of hybridization is verified by the 0.67, 0.78 and 0.95 eV gaps between the d-band centers of Pd and Ni on $Pd_1Ni_{0.33}(111)$, $Pd_1Ni_1(111)$ and $Pd_1Ni_3(111)$, respectively. This suggests that electronic stimulation of FA dehydrogenation is greater on $Pd_1Ni_1(111)$ and $Pd_1Ni_{0.33}(111)$ than it is on $Pd_1Ni_3(111)$, which is structurally more perturbed by greater amounts of Ni. This phenomenon may explain the volcano-type activity obtained experimentally with $Pd_1Ni_{0.37}$, $Pd_1Ni_{1.3}$ and $Pd_1Ni_{3.6}$ in Fig. 3b, and is supported by a recent report that the elevated catalytic activity observed experimentally for CO oxidation over Pd_1Ni_1 arises from increased interactions among adjacent Pd and Ni atoms based on HE-XRD/PDFs and a Monte Carlo simulation.[51] The balance point and calculation methods for the gaps is shown in ESI,† Section S2.

3.3.3. Adsorption sites for key intermediates. We selected $Pd_1Ni_1(111)$ to represent the surface of the $Pd_1Ni_{1.3}$ alloy showing the greatest catalytic activity to understand the origin of its elevated activity relative to Pd(111). Preferred adsorption sites for reaction intermediates were explored on Pd(111) and $Pd_1Ni_1(111)$ surfaces. The key intermediates produced by FA dehydrogenation include HCOOH, HCOO, COOH, CO, OH and H.[61–64] Plausible adsorption sites were chosen as atop, bridge, hollow (hcp) and hollow (fcc) positions on the Pd(111) surface and enlarged to include atop-Pd, atop-Ni, bridge-Pd–Pd, bridge-Pd–Ni, bridge-Ni–Ni, hollow (hcp)-Pd_1Ni_2, hollow (hcp)-Pd_2Ni_1, hollow (fcc)-Pd_1Ni_2 and hollow (fcc)-Pd_2Ni_1 positions on the $Pd_1Ni_1(111)$ surface (Fig. S5, ESI†). The calculated adsorption energies of the key intermediate species are listed in Tables S9–S13 (ESI†). The results show that the atop-Ni, bridge-Ni–Ni, hollow (hcp)-Pd_1Ni_2, hollow (fcc)-Pd_1Ni_2 sites are more favorable than the atop-Pd, bridge-Pd–Ni, bridge-Pd–Pd, hollow (hcp)-Pd_2Ni_1 and hollow (fcc)-Pd_2Ni_1 positions for

adsorption of key intermediates. The d-band center calculations suggest that the active sites on the $Pd_1Ni_1(111)$ surface are closely associated with the Pd–Ni configuration; a Pd atom likely interacts with an adjacent Ni atom to induce charge transfer, which agrees well with the XPS results.

Adsorbates are bound primarily at the Ni atoms on the $Pd_1Ni_1(111)$ surface. This result is attributed in part to the difference in metal electronegativity. Carbon-containing adsorbates will interact more strongly with Ni than with Pd, because the electronegativity of Ni is smaller.[65] This implies that electron charge transfer from Ni to C in key intermediates is easier than from Pd to C. The Pauling electronegativities of Ni, Pd, H, C and O are 1.91, 2.20, 2.20, 2.55 and 3.44, respectively. The calculated binding affinity of intermediates on the Pd(111) surfaces increases (i.e., the adsorption energy becomes more negative) in the order HCOOH < H ≪ $HCOO_b$ < CO < COOH < $HCOO_a$ < OH (Table S9, ESI†). The binding affinity is greater on the $Pd_1Ni_1(111)$ surface than it is on Pd(111) for all key intermediates except CO* and H* (Table S9, ESI†). The adsorption strength of intermediates on the $Pd_1Ni_1(111)$ surface increases as: HCOOH < H ≪ CO < $HCOO_b$ < COOH < $HCOO_a$ < OH. The adsorption configurations are shown in Fig. S7 (ESI†). HCOOH is preferentially adsorbed in the *trans* rather than *cis* conformation, which has been confirmed by theoretical and experimental studies.[61–64,66] $HCOO_a$ has a high binding affinity on both surfaces due to the strong interaction between the metal surface and the two oxygen atoms of HCOO (Fig. S7, ESI†). The adsorption configuration of $HCOO_b$ leads to the formation of metal–O and metal–H bonds and to weaker binding energies than with $HCOO_a$ (Fig. S7, ESI†).

The initial adsorption configuration of a reactant may strongly influence the entire pathway of a reaction in the NEB calculation. Therefore, we calculated the geometrical parameters of relevant adsorbates as a function of their configurations. The calculated parameters of the O–H, C–H, C=O and C–O bonds in gas-phase HCOOH, HCOOH*, $HCOO_a$*, $HCOO_b$* and COOH* on Pd(111) and $Pd_1Ni_1(111)$ surfaces are listed in Table S8 (ESI†). The asterisk (*) denotes adsorbed species. Compared to gas-phase HCOOH, the adsorbed HCOOH* configurations on Pd(111) and $Pd_1Ni_1(111)$ surfaces show variations in their O–H and C–H bond lengths. The O–H bonds of HCOOH* are stretched by 3.19 and 3.84%, whereas the C–H bonds are compressed by 0.21 and 0.32% on the Pd(111) and $Pd_1Ni_1(111)$ surfaces, respectively. The elongation of O–H bonds of both surfaces suggests that O–H bond scission is the initial step in the production of H* and HCOO* from HCOOH* (HCOOH* → HCOO* + H*). The C–H bond lengths in $HCOO_a$* are nearly identical at 1.110 Å on Pd(111) and 1.107 Å on $Pd_1Ni_1(111)$, but the corresponding bonds in $HCOO_b$* are elongated by 6.45 and 1.34% on Pd(111) and $Pd_1Ni_1(111)$, respectively. Given the geometric information and binding affinities of $HCOO_a$* and $HCOO_b$* for metal surfaces, it is plausible that the HCOO* produced in the initial dehydrogenation of HCOOH is first bound to the surface as $HCOO_a$*. However, actual C–H bond activation may occur *via* $HCOO_b$* to produce CO_2 and H* by the following process: $HCOO_a$* + H* → $HCOO_b$* + H* →

This journal is © the Owner Societies 2021

Phys. Chem. Chem. Phys., 2021, **23**, 11515–11527 | **11521**

$CO_2 + 2H^*$. This suggests the likely interconversion of $HCOO_a^*$ to $HCOO_b^*$ (*vide infra*). The two H^* species produced in this process recombine to release a hydrogen molecule: $H^* + H^* \rightarrow H_2$. To validate the foregoing hypothesis, plausible mechanisms of FA dehydrogenation were further explored by calculating the activation energies of relevant transition states in the reaction pathways.

3.3.4. Plausible reaction pathways of FA dehydrogenation. A schematic representation of probable FA dehydrogenation pathways is presented in Fig. 5. The first dehydrogenation of HCOOH* (**I**) can produce either a formate (HCOO) or carboxyl (COOH) intermediate. The HCOO intermediate is initially adsorbed onto the surface as $HCOO_a + H^*$ (**II**), which proceeds directly to C–H bond breaking through TS_2 yielding $CO_2^* + 2H^*$ (**III**) or is converted into the $HCOO_b$ configuration (**IV**) *via* TS_3 producing $CO_2^* + 2H^*$ (**III**) by C–H bond cleavage through TS_4. Alternatively, the COOH* intermediate (**V**) following C–H bond activation through TS_5 decomposes into $CO_2^* + 2H^*$ (**III**) *via* O–H bond cleavage through TS_6 or decomposes into $CO^* + OH^*$ (**VI**) *via* C–O bond scission through TS_7.

3.3.4.1. FA dehydrogenation initiated by O–H bond scission (HCOO pathway). HCOOH dehydrogenation initiated by O–H bond cleavage produces the $HCOO_a$ intermediate (**II**). The geometries of HCOOH* ground state structures at Pd(111) and Pd_1Ni_1(111) surfaces (Table S8, ESI†) suggest that the O–H bonds of adsorbed HCOOH* are partially activated at both surfaces. This is supported by bond elongations of 3.19 and 3.84% on Pd(111) and Pd_1Ni_1(111), respectively. Fig. 6a shows the steps and activation energies of FA dehydrogenation by the HCOO pathway based on the initial $HCOO_a^*$ configuration.

The first step in the HCOO pathway is activation of the O–H bond of HCOO–H* to form $HCOO_a^* + H^*$ (**II**) *via* TS_1 with activation energies of 0.78 and 0.61 eV for Pd(111) and
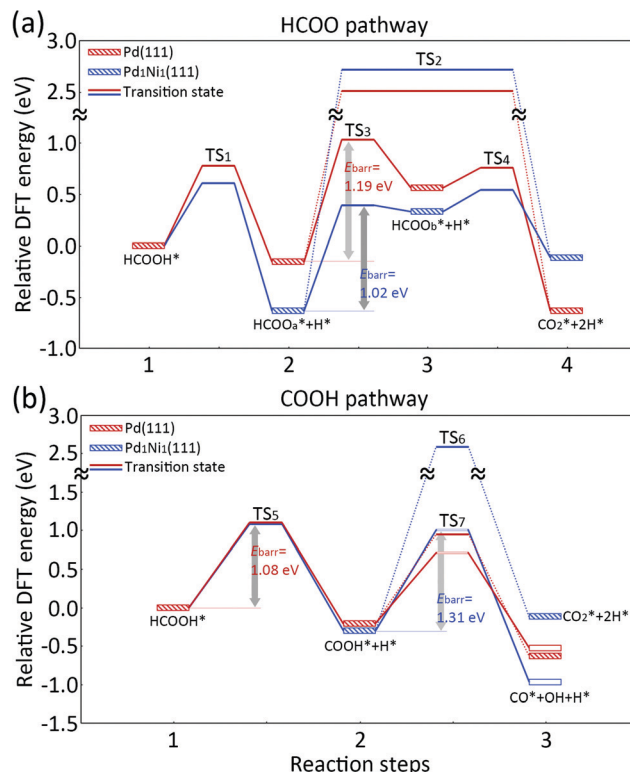
Fig. 6 Relative DFT energy diagrams for FA dehydrogenation proceeding by the (a) HCOO and (b) COOH pathways over Pd(111) (red) and Pd_1Ni_1(111) (blue) surfaces. The solid and dashed lines indicate the $I \rightarrow II \rightarrow IV \rightarrow III$ and $I \rightarrow II \rightarrow III$ steps in the HCOO pathway and the $I \rightarrow V \rightarrow VI$ and $I \rightarrow V \rightarrow III$ steps in the COOH pathway, respectively, according to the notation in Fig. 5.

Pd_1Ni_1(111), respectively (Table 1). The most stable configuration of the adsorbed $HCOO_a^*$ intermediate has two Pd–O bonds on Pd(111) and two Ni–O bonds on Pd_1Ni_1(111). Other adsorption configurations comprising two Pd–O bonds and one Pd–O plus one Ni–O bond were optimized on Pd_1Ni_1(111), but these configurations were less stable than the intermediate with two Ni–O bonds (Fig. S7c, ESI†). The $HCOO_a^*$ intermediate is converted into $CO_2^* + 2H^*$ (**III**) *via* C–H bond scission, which can proceed in two ways. The first path is direct C–H bond activation *via* TS_2 yielding $CO_2^* + 2H^*$ (**III**), which requires greater activation energies of 2.66 and 3.34 eV on Pd(111) and Pd_1Ni_1(111) surfaces, respectively (dashed lines in Fig. 6a). The other path involves rotational conversion of $HCOO_a^* + H^*$ (**II**) into $HCOO_b^* + H^*$ (**IV**) *via* TS_3 followed by C–H bond activation *via* TS_4 to produce $CO_2^* + 2H^*$ (**III**) (solid lines in Fig. 6a). The conformational rotation of $HCOO_a^*$ requires activation energies of 1.19 eV on Pd(111) and 1.02 eV on Pd_1Ni_1(111). The $HCOO_b^* + H^*$ (**IV**) intermediate produced by rotation of $HCOO_a^* + H^*$ (**II**) has one Pd–O bond and one Pd–H bond on Pd(111) and one Ni–O bond and one Ni–H bond on Pd_1Ni_1(111) (Fig. 5 and Fig. S7c, ESI†). The consecutive C–H bond cleavage requires activation energies of 0.19 and 0.21 eV on Pd(111) and Pd_1Ni_1(111) surfaces, respectively. These results clearly indicate that the energetically lower HCOO pathway involves interconversion from HCOOH* (**I**) $\rightarrow HCOO_a^* + H^*$ (**II**) $\rightarrow HCOO_b^* + H^*$ (**IV**) to $CO_2^* + 2H^*$ (**III**). The greater activation

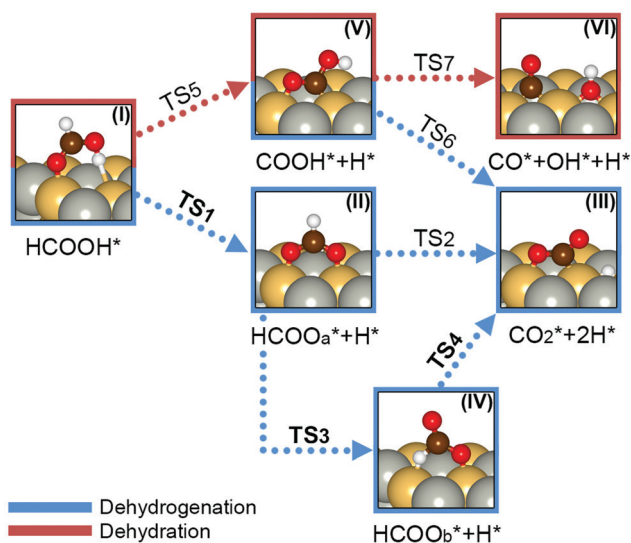**Fig. 5** Schematic representation of probable reaction pathways of FA dehydrogenation at the Pd_1Ni_1(111) surface. Dashed blue and red lines indicate dehydrogenation and dehydration reactions, respectively. Grey, light yellow, dark brown, red and white spheres represent Pd, Ni, C, O and H atoms, respectively.
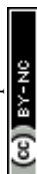
Table 1 Calculated activation energies for FA decomposition *via* the HCOO and COOH pathways on Pd(111) and Pd_1Ni_1(111) surfaces. The intermediate species **I–VI** and transition states TS_1–TS_7 are defined in Fig. 5

HCOO pathway		TS_1 (eV) (**I → II**)	TS_2 (eV) (**II → III**)	TS_3 (eV) (**II → IV**)	TS_4 (eV) (**IV → III**)
I → II → III	Pd(111)	0.78	2.66	—	—
	Pd_1Ni_1(111)	0.61	3.34	—	—
I → II → IV → III	Pd(111)	0.78	—	1.19	0.19
	Pd_1Ni_1(111)	0.61	—	1.02	0.21

COOH pathway		TS_5 (eV) (**I → V**)	TS_6 (eV) (**V → III**)	TS_7 (eV) (**V → VI**)
I → V → III	Pd(111)	1.08(5)	1.15	—
	Pd_1Ni_1(111)	1.07(6)	2.89	—
I → V → VI	Pd(111)	1.08(5)	—	0.92
	Pd_1Ni_1(111)	1.07(6)	—	1.31

energy for the direct C–H bond scission of $HCOO_a$* is related to the unreactive character of its C–H bond at both surfaces, as evident from the negligible change in C–H bond length of adsorbed $HCOO_a$* (Table S8, ESI†). These results further indicate that the rate determining step in the HCOO pathway of FA dehydrogenation on Pd(111) and Pd_1Ni_1(111) lies in the TS_3 step involving rotation of $HCOO_a$* to $HCOO_b$*. This interpretation is in line with recent studies of FA dehydrogenation, which favor the rate limiting step of HCOO* + H* → CO_2* + 2H* rather than HCOOH* → HCOO* + H*.[67–69]

3.3.4.2. FA dehydrogenation initiated by C–H bond scission (COOH and CO–OH pathways). HCOOH dehydrogenation *via* the COOH pathway is initiated by C–H bond scission and produces the COOH* intermediate. The C–H bond cleavage of HCOOH* *via* TS_5 on Pd(111) and Pd_1Ni_1(111) surfaces requires greater activation energies of 1.085 and 1.076 eV, respectively (Table 1 and solid lines in Fig. 6b), than those of TS_1. This view is supported by the compressed C–H bond of HCOOH* on Pd_1Ni_1(111) as well as the identical C–H bond length on Pd(111) (Table S8, ESI†). The HCOO pathway is favored over the COOH pathway on both surfaces. The COOH* species (**V**) in Fig. 5 can further be dehydrogenated by O–H bond cleavage *via* TS_6 generating CO_2* + 2H* (**III**) (dashed lines in Fig. 6b) or dehydrated by C–O bond cleavage *via* TS_7 yielding CO* + OH* (**VI**) (solid lines in Fig. 6b). The barrier to O–H bond breaking (TS_6) on both surfaces is greater than that of TS_5. The activation energies of TS_6 on Pd(111) and Pd_1Ni_1(111) are 1.15 and 2.89 eV, respectively. The kinetic barriers to C–O bond cleavage [TS_7: 0.92 eV on Pd(111), 1.31 eV on Pd_1Ni_1(111)] are lower than those of TS_6 at these surfaces. This indicates that the dehydration reaction (C–O bond cleavage) is favored over the dehydrogenation reaction (O–H bond cleavage) in the COOH pathway. Despite these negative findings, it is important that the activation energy of TS_7 on Pd_1Ni_1(111) is greater than it is on Pd(111). This means that the Pd_1Ni_1(111) surface will have greater ability than the Pd(111) surface to control CO production.

The calculated energy diagrams in Fig. 6 reveal that the HCOO pathway is the most favorable HCOOH dehydrogenation pathway through the conversion of $HCOO_a$* to $HCOO_b$*. It is evident that the Pd_1Ni_1(111) catalyst displays lower kinetic barriers

to the desired reaction than the Pd(111) catalyst. Thus, the computational results agree well with the experimental results that demonstrate the improved activity of PdNi/N–C compared to Pd/C for H_2-release from aqueous FA solution (Fig. 3).

3.3.4.3. FA dehydrogenation on $Pd_1Ni_{0.33}$(111) and Pd_1Ni_3(111) surfaces. We further confirmed that HCOOH dehydrogenation is more favorable on Pd_1Ni_x(111) surfaces than on Pd(111) by analyzing the activation energies of key steps in the optimal HCOO pathway and the initial step of the COOH pathway on $Pd_1Ni_{0.33}$(111) and Pd_1Ni_3(111) surfaces (Fig. 7 and Table S14, ESI†). The activation energies of the HCOO pathway [HCOOH* (**I**) → $HCOO_a$* + H* (**II**) → $HCOO_b$* + H* (**IV**) → CO_2* + H* (**III**)] and the initial step of the COOH pathway [HCOOH* (**I**) → COOH* + H* (**V**)] on $Pd_1Ni_{0.33}$(111) and Pd_1Ni_3(111) demonstrate the favorability of the HCOO pathway [TS_1: $Pd_1Ni_{0.33}$(111) = 0.77 eV, Pd_1Ni_3(111) = 0.60 eV] over the COOH pathway [TS_5: 0.78 and 0.74 eV, respectively] (Fig. 7 and Table S14, ESI†). In the rate determining step (TS_3), $Pd_1Ni_{0.33}$(111) (0.86 eV) and Pd_1Ni_3(111) (1.16 eV) exhibit lower activation energies than the Pd(111) surface (1.19 eV) (Fig. 7).

Interestingly, the $Pd_1Ni_{0.33}$(111) surface has the lowest energy barrier for the rate determining step among the Pd_1Ni_x(111) surfaces. This disagrees with the trend in efficiency of HCOOH dehydrogenation determined by our experimental findings ($Pd_1Ni_{1.3}$/N–C > $Pd_1Ni_{0.37}$/N–C > $Pd_1Ni_{3.6}$/N–C > Pd/N–C; Fig. 3b). However, there is a very small difference between the activation energies of the initial steps in the HCOO and COOH pathways (0.77 and 0.78 eV, respectively) at the $Pd_1Ni_{0.33}$(111) surface. This may lead to CO production *via* a side reaction in the COOH pathway due to poor selectivity between the HCOO and COOH mechanisms resulting in a decrease in the measured efficiency of HCOOH dehydrogenation. Similar cases have been reported in previous studies.[63,68,70] These facts inspired us to analyze the detailed properties of Pd_1Ni_x(111) surfaces to assess the efficiency of HCOOH dehydrogenation on each material.

3.4. Key factors of Pd_1Ni_x(111) surfaces for enhancing FA dehydrogenation

Alloying Pd with Ni produces electronic and geometric effects arising from the relatively smaller electronegativity and lattice
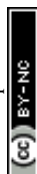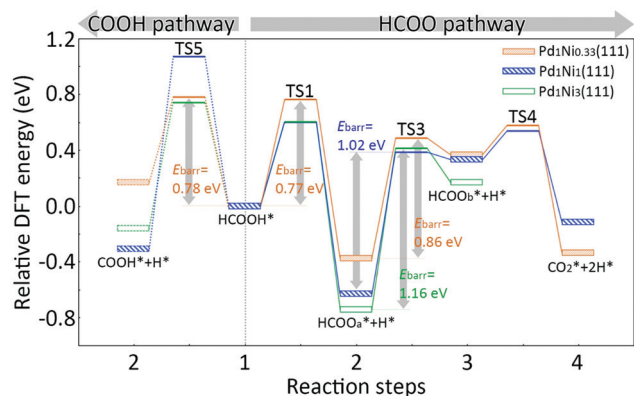
Fig. 7 Relative DFT energy diagram for FA dehydrogenation proceeding by the optimal HCOO pathway (I → II → IV → III steps, right) and the COOH pathway (initial step only, left) over $Pd_1Ni_{0.33}(111)$ (orange), $Pd_1Ni_1(111)$ (blue) and $Pd_1Ni_3(111)$ (green) surfaces.

adsorbates interact directly with Ni atoms on the catalyst surfaces. The O atom with the greatest electronegativity prefers to interact with the relatively less electronegative Ni than Pd because electron transfer from O to the metal is easier.

We also found changes in the electronic properties of catalysts depending on the amount of Ni in Pd_1Ni_x alloys by calculating work functions and spin densities of the four catalyst surfaces. The work function values of Pd(111), $Pd_1Ni_{0.33}(111)$, $Pd_1Ni_1(111)$ and $Pd_1Ni_3(111)$ surfaces are 5.57, 5.30, 5.19 and 5.20 eV, respectively. Generally, the reduction in work function with increasing Ni content indicates easier electron transfer from the catalyst to adsorbate, which leads to a stronger adsorption interaction. Higher Ni content in Pd_1Ni_x also produces greater spin densities on the surface layers of the catalysts (Fig. S7, ESI†), which can trigger strong adsorption.[59,60] An interesting finding is that the differences in adsorption strength of intermediates on Pd(111) surface and $Pd_1Ni_x(111)$ surfaces were clearly attributed to the electronic properties, whereas those were not among $Pd_1Ni_x(111)$ surfaces. These results mean that the electronic properties of Pd_1Ni_x alloys play an important role in the formation of intermediates on catalyst surfaces as evidenced by the more favorable adsorption of HCOOH and other intermediates on

constants of Ni, respectively, which may affect HCOOH dehydrogenation in positive ways. Fig. 8 and Table S15 (ESI†) show that the key adsorbates in the HCOOH dehydrogenation reaction pathways are significantly influenced by the electronic effect of $Pd_1Ni_x(111)$ surfaces, especially when the O atoms of
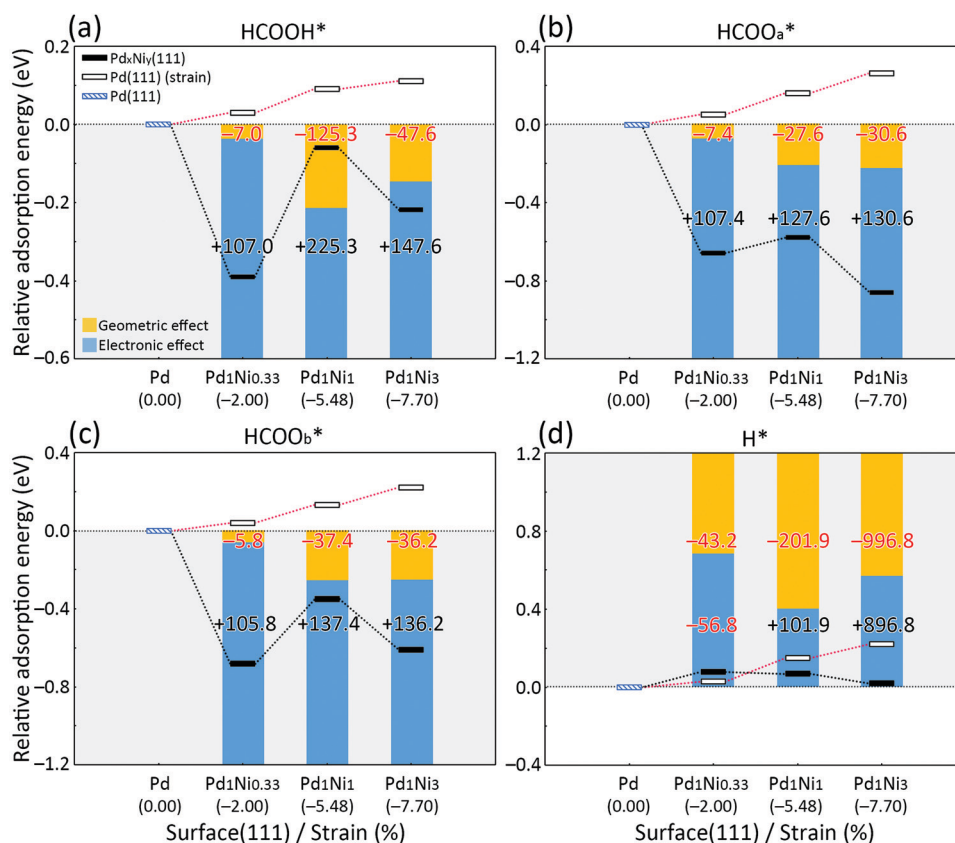
Fig. 8 Relative adsorption energy diagrams of (a) HCOOH*, (b) $HCOO_a$*, (c) $HCOO_b$* and (d) H* as a function of surface composition and strain. The small blue, black and white rectangles represent the relative adsorption energy of adsorbates on Pd(111), $Pd_1Ni_x(111)$ and compressed Pd(111) surfaces, respectively. The yellow and blue bars indicate the relative contributions of geometric and electronic effects on the adsorption strength at Pd_1Ni_x alloys; positive (black) and negative (red) values (%) indicate increasing and decreasing contributions to the strength of adsorption. The numbers in parentheses on the x-axis represent the percent compressive strain.

11524 | *Phys. Chem. Chem. Phys.*, 2021, **23**, 11515–11527

This journal is © the Owner Societies 2021

$Pd_1Ni_x(111)$ than on $Pd(111)$ surfaces, and also imply the existence of possibility that other factors like geometric properties may affect the adsorption of adsorbates.

Adsorbates such as CO and H are adsorbed more weakly on $Pd_1Ni_x(111)$ than on $Pd(111)$ (Table S9, ESI†). Because CO and H do not have an O atom that strongly interacts with the catalyst surfaces due to its high electronegativity, these adsorbates may be more influenced by factors beyond electronic effects unlike HCOOH, $HCOO_a$ and $HCOO_b$ (Fig. 8). Fig. 8d demonstrates that for H adsorption on PdNi surfaces the geometric effect is greater than the electronic effect relative to the behavior of other adsorbates (Fig. 8a–c). In the case of HCOOH dehydrogenation, which depends on the weak adsorption of hydrogen, desorption of H* from the surface may be an important step in producing $H_{2(g)}$ as the final product.[60] The most stable adsorption configurations of H* on $Pd(111)$, $Pd_1Ni_{0.33}(111)$, $Pd_1Ni_1(111)$ and $Pd_1Ni_3(111)$ are shown in Fig. S10 (ESI†). The calculated adsorption energies are −0.60, −0.52, −0.53 and −0.58, respectively. The results do not correlate with the amount of Ni. An interesting and important finding is that—although electron transfer from the catalyst surface to H* increases with increasing Ni content as 0.11, 0.17, 0.21 and 0.26 e—H* exhibits weaker adsorption energies on the $Pd_1Ni_{0.33}(111)$ and $Pd_1Ni_1(111)$ surfaces that simulate the $Pd_1Ni_{0.37}$ and $Pd_1Ni_{1.3}$ catalysts, which show excellent FA dehydrogenation efficiency in our experiments. This evidence supports the assumption that factors other than electronic effects may influence FA dehydrogenation. Fig. 8d shows that electronic effects on H* adsorption are weak relative to adsorption of other substrates.

An important factor in FA dehydrogenation is the compressive strain caused by geometric differences in the lattice constants of Pd and Ni. To assess the contribution of this factor, we applied compressive strain to $Pd(111)$ surfaces in increments of 2.00, 5.48 and 7.70% from the interatomic distances on a $Pd(111)$ surface (0% compressive strain) and subsequently calculated the H* adsorption energies and conducted an excess Bader charge analysis. The strength of H* adsorption decreases to −0.57, −0.45 and −0.38 eV (Table S16, ESI† and Fig. 8d), and the electronic charge transferred from the surface to H* decreases to 0.118, 0.095 and 0.089 e as the compressive strain increases. Fig. 8a–c show that the adsorption strength of O-containing adsorbates (HCOOH, $HCOO_a$ and $HCOO_b$) also decreases as the interatomic distance decreases, which agrees with previous studies.[71,72] Detailed adsorption energies of these forms are collected in Table S16 (ESI†). The results indicate that addition of an appropriate amount of Ni to Pd can lower the activation energy for the FA dehydrogenation and enhance the reaction rate based on (i) the stable formation of key O-containing intermediates (an electronic effect) that interact directly with the surface (Fig. 8a–c) and (ii) weakened H* adsorption (a geometric effect), which facilitates more favorable H* desorption to produce $H_{2(g)}$ (Fig. 8d). $Pd_1Ni_1(111)$ exhibits the most appropriate electronic and geometric properties for FA dehydrogenation among the $Pd(111)$, $Pd_1Ni_{0.33}(111)$, $Pd_1Ni_1(111)$ and $Pd_1Ni_3(111)$ surfaces. This conclusion is supported by the result that

$Pd_1Ni_1(111)$ presents the lowest activation barrier to H* desorption (2.80 eV) based on single point calculations of the four catalyst surfaces (Fig. S11, ESI†). It is also true that the energetic span (sum of endothermic reactions) from DFT calculations on the $Pd_1Ni_1(111)$ surface (1.84 eV) in the overall HCOO pathway including the CO_2* + 2H* formation step (TS_4) leading to $H_{2(g)}$ production is slightly lower than that of $Pd_1Ni_{0.33}(111)$ (1.85 eV) (Fig. 7).

4. Conclusions

Experimental and theoretical studies demonstrate that Pd–Ni alloys possess greater catalytic activities towards FA dehydrogenation than Pd metal. Electronic structural studies using XPS and d-band center calculations show that catalytic dehydrogenation activities improve as a result of synergistic interactions between Pd and Ni atoms, which suggests that the active site of FA dehydrogenation is associated with both Pd and Ni atoms rather than either metal alone. The heterogeneous Pd–Ni structure also plays a synergistic role in improving catalytic activity based on constructive delocalization of Pd and Ni d-bands. The improved catalytic activity of Pd_1Ni_x/N–C (x = 0.37, 1.3 and 3.6) in FA dehydrogenation at ambient temperature is supported by calculations employing the DFT-NEB method. The HCOO pathway is favored over the COOH/CO–OH pathway at both Pd and Pd_1Ni_1 surfaces, which indicates that the as-prepared catalyst prefers the dehydrogenation over the dehydration pathway. Finally, the PdNi catalyst with the appropriate amount of Ni (*i.e.*, the Pd_1Ni_1 catalyst in the DFT calculations) showed the highest catalytic activity not only by lowering the activation energy along the pathway of FA dehydrogenation reaction but also by suppressing the side reaction of CO production. The fundamental understanding of FA dehydrogenation over PdNi-alloy catalysts presented herein should contribute to the design of novel, highly capable, and inexpensive heterogeneous catalysts to achieve the rapid H_2-release from FA for numerous hydrogen energy applications.

Conflicts of interest

There are no conflicts to declare.

Acknowledgements

References

1 S. Chu and A. Majumdar, *Nature*, 2012, **488**, 294–303.
2 E. B. Fox, Z.-W. Liu and Z.-T. Liu, *Energy Fuels*, 2013, **27**, 6335–6338.

This journal is © the Owner Societies 2021

Phys. Chem. Chem. Phys., 2021, **23**, 11515–11527 | 11525
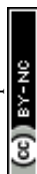
3 N. Armaroli and V. Balzani, *Angew. Chem., Int. Ed.*, 2007, **46**, 52–66.

4 G. A. Olah, *Angew. Chem., Int. Ed.*, 2005, **44**, 2636–2639.

5 P. Preuster, C. Papp and P. Wasserscheid, *Acc. Chem. Res.*, 2017, **50**, 74–85.

6 A. Boddien, F. Gärtner, C. Federsel, P. Sponholz, D. Mellmann, R. Jackstell, H. Junge and M. Beller, *Angew. Chem., Int. Ed.*, 2011, **50**, 6411–6414.

7 F. Bonaccorso, L. Colombo, G. Yu, M. Stoller, V. Tozzini, A. C. Ferrari, R. S. Ruoff and V. Pellegrini, *Science*, 2015, **347**, 1246501.

8 D. J. Durbin and C. Malardier-Jugroot, *Int. J. Hydrogen Energy*, 2013, **38**, 14595–14617.

9 P. P. Edwards, V. L. Kuznetsov, W. I. F. David and N. P. Brandon, *Energy Policy*, 2008, **36**, 4356–4362.

10 L. Schlapbach and A. Züttel, *Nature*, 2001, **414**, 353–358.

11 M. Reuß, T. Grube, M. Robinius, P. Preuster, P. Wasserscheid and D. Stolten, *Appl. Energy*, 2017, **200**, 290–302.

12 N. Armaroli and V. Balzani, *ChemSusChem*, 2011, **4**, 21–36.

13 J. Graetz, *Chem. Soc. Rev.*, 2009, **38**, 73–82.

14 F. Joó, *ChemSusChem*, 2008, **1**, 805–808.

15 K. Jiang, K. Xu, S. Zou and W.-B. Cai, *J. Am. Chem. Soc.*, 2014, **136**, 4861–4864.

16 J. H. Lee, J. Ryu, J. Y. Kim, S.-W. Nam, J. H. Han, T.-H. Lim, S. Gautam, K. H. Chae and C. W. Yoon, *J. Mater. Chem. A*, 2014, **2**, 9490–9495.

17 F.-Z. Song, Q.-L. Zhu, N. Tsumori and Q. Xu, *ACS Catal.*, 2015, **5**, 5141–5144.

18 J. F. Hull, Y. Himeda, W.-H. Wang, B. Hashiguchi, R. Periana, D. J. Szalda, J. T. Muckerman and E. Fujita, *Nat. Chem.*, 2012, **4**, 383–388.

19 K. Koh, J. E. Seo, J. H. Lee, A. Goswami, C. W. Yoon and T. Asefa, *J. Mater. Chem. A*, 2014, **2**, 20444–20449.

20 A. Álvarez, A. Bansode, A. Urakawa, A. V. Bavykina, T. A. Wezendonk, M. Makkee, J. Gascon and F. Kapteijn, *Chem. Rev.*, 2017, **117**, 9804–9838.

21 T. Asefa, K. Koh and C. W. Yoon, *Adv. Energy Mater.*, 2019, **9**, 1901158.

22 Y. Kim and D. H. Kim, *Appl. Catal., B*, 2019, **244**, 684–693.

23 H.-j. Jeon and Y.-M. Chung, *Appl. Catal., B*, 2017, **210**, 212–222.

24 S. Akbayrak, Y. Tonbul and S. Özkar, *Appl. Catal., B*, 2017, **206**, 384–392.

25 M. Hattori, H. Einaga, T. Daio and M. Tsuji, *J. Mater. Chem. A*, 2015, **3**, 4453–4461.

26 K. Tedsree, T. Li, S. Jones, C. W. A. Chan, K. M. K. Yu, P. A. J. Bagot, E. A. Marquis, G. D. W. Smith and S. C. E. Tsang, *Nat. Nanotechnol.*, 2011, **6**, 302–307.

27 Y. Huang, X. Zhou, M. Yin, C. Liu and W. Xing, *Chem. Mater.*, 2010, **22**, 5122–5128.

28 Z.-L. Wang, J.-M. Yan, H.-L. Wang, Y. Ping and Q. Jiang, *J. Mater. Chem. A*, 2013, **1**, 12721–12725.

29 Y.-L. Qin, J. Wang, F.-Z. Meng, L.-M. Wang and X.-B. Zhang, *Chem. Commun.*, 2013, **49**, 10028–10030.

30 Y.-L. Qin, Y.-C. Liu, F. Liang and L.-M. Wang, *ChemSusChem*, 2015, **8**, 260–263.

31 C. Hu, X. Mu, J. Fan, H. Ma, X. Zhao, G. Chen, Z. Zhou and N. Zheng, *ChemNanoMat*, 2016, **2**, 28–32.

32 Ö. Metin, X. Sun and S. Sun, *Nanoscale*, 2013, **5**, 910–912.

33 W.-Y. Yu, G. M. Mullen, D. W. Flaherty and C. B. Mullins, *J. Am. Chem. Soc.*, 2014, **136**, 11070–11078.

34 Z.-L. Wang, J.-M. Yan, Y. Ping, H.-L. Wang, W.-T. Zheng and Q. Jiang, *Angew. Chem., Int. Ed.*, 2013, **52**, 4406–4409.

35 H. Wang, Y. Chi, D. Gao, Z. Wang, C. Wang, L. Wang, M. Wang, D. Cheng, J. Zhang, C. Wu and Z. Zhao, *Appl. Catal., B*, 2019, **255**, 117776.

36 G. Kresse and J. Furthmüller, *Phys. Rev. B: Condens. Matter Mater. Phys.*, 1996, **54**, 11169–11186.

37 G. Kresse and J. Hafner, *Phys. Rev. B: Condens. Matter Mater. Phys.*, 1993, **47**, 558–561.

38 J. Hafner, *J. Comput. Chem.*, 2008, **29**, 2044–2078.

39 P. E. Blöchl, *Phys. Rev. B: Condens. Matter Mater. Phys.*, 1994, **50**, 17953–17979.

40 G. Kresse and D. Joubert, *Phys. Rev. B: Condens. Matter Mater. Phys.*, 1999, **59**, 1758–1775.

41 J. P. Perdew, J. A. Chevary, S. H. Vosko, K. A. Jackson, M. R. Pederson, D. J. Singh and C. Fiolhais, *Phys. Rev. B: Condens. Matter Mater. Phys.*, 1992, **46**, 6671–6687.

42 J. P. Perdew, J. A. Chevary, S. H. Vosko, K. A. Jackson, M. R. Pederson, D. J. Singh and C. Fiolhais, *Phys. Rev. B: Condens. Matter Mater. Phys.*, 1993, **48**, 4978.

43 H. J. Monkhorst and J. D. Pack, *Phys. Rev. B: Solid State*, 1976, **13**, 5188–5192.

44 M. Methfessel and A. T. Paxton, *Phys. Rev. B: Condens. Matter Mater. Phys.*, 1989, **40**, 3616–3621.

45 D. Sheppard, R. Terrell and G. Henkelman, *J. Chem. Phys.*, 2008, **128**, 134106.

46 D. Sheppard, P. Xiao, W. Chemelewski, D. D. Johnson and G. Henkelman, *J. Chem. Phys.*, 2012, **136**, 074103.

47 R. F. W. Bader, *Chem. Rev.*, 1991, **91**, 893–928.

48 W. Tang, E. Sanville and G. Henkelman, *J. Phys.: Condens. Matter*, 2009, **21**, 084204.

49 P. Lu, T. Teranishi, K. Asakura, M. Miyake and N. Toshima, *J. Phys. Chem. B*, 1999, **103**, 9673–9682.

50 Q. Guo, D. Liu, X. Zhang, L. Li, H. Hou, O. Niwa and T. You, *Anal. Chem.*, 2014, **86**, 5898–5905.

51 S. Shan, V. Petkov, L. Yang, J. Luo, P. Joseph, D. Mayzel, B. Prasai, L. Wang, M. Engelhard and C.-J. Zhong, *J. Am. Chem. Soc.*, 2014, **136**, 7140–7151.

52 J. L. Santos, C. León, G. Monnier, S. Ivanova, M. Á. Centeno and J. A. Odriozola, *Int. J. Hydrogen Energy*, 2020, **45**, 23056–23068.

53 S. Zhang, Ö. Metin, D. Su and S. Sun, *Angew. Chem., Int. Ed.*, 2013, **52**, 3681–3684.

54 I. A. Pašti, N. M. Gavrilov and S. V. Mentus, *Electrochim. Acta*, 2014, **130**, 453–463.

55 S. Bhattacharjee, S. J. Yoo, U. V. Waghmare and S. C. Lee, *Chem. Phys. Lett.*, 2016, **648**, 166–169.

56 J. H. Lee, S. Kattel, Z. Jiang, Z. Xie, S. Yao, B. M. Tackett, W. Xu, N. S. Marinkovic and J. G. Chen, *Nat. Commun.*, 2019, **10**, 3724.

57 H. Asonen, C. Barnes, A. Salokatve and A. Vuoristo, *Appl. Surf. Sci.*, 1985, **22-23**, 556–564.

11526 | *Phys. Chem. Chem. Phys.*, 2021, **23**, 11515–11527

This journal is © the Owner Societies 2021

58 A. Staykov, T. Kamachi, T. Ishihara and K. Yoshizawa, *J. Phys. Chem. C*, 2008, **112**, 19501–19505.

59 L. Zhang and Z. Xia, *J. Phys. Chem. C*, 2011, **115**, 11170–11176.

60 D. Y. Shin, M.-S. Kim, J. A. Kwon, Y.-J. Shin, C. W. Yoon and D.-H. Lim, *J. Phys. Chem. C*, 2019, **123**, 1539–1549.

61 C. Hu, S.-W. Ting, K.-Y. Chan and W. Huang, *Int. J. Hydrogen Energy*, 2012, **37**, 15956–15965.

62 Y. Wang, Y. Qi, D. Zhang and C. Liu, *J. Phys. Chem. C*, 2014, **118**, 2067–2076.

63 J. A. Herron, J. Scaranto, P. Ferrin, S. Li and M. Mavrikakis, *ACS Catal.*, 2014, **4**, 4434–4445.

64 J. S. Yoo, F. Abild-Pedersen, J. K. Nørskov and F. Studt, *ACS Catal.*, 2014, **4**, 1226–1233.

65 J. A. Kwon, M.-S. Kim, D. Y. Shin, J. Y. Kim and D.-H. Lim, *J. Ind. Eng. Chem.*, 2017, **49**, 69–75.

66 W. H. Hocking, *Z. Naturforsch., A: Phys., Phys. Chem., Kosmophys.*, 1976, **31**, 1113–1121.

67 J. Cho, S. Lee, J. Han, S. P. Yoon, S. W. Nam, S. H. Choi, K.-Y. Lee and H. C. Ham, *J. Phys. Chem. C*, 2014, **118**, 22553–22560.

68 J. Cho, S. Lee, S. P. Yoon, J. Han, S. W. Nam, K.-Y. Lee and H. C. Ham, *ACS Catal.*, 2017, **7**, 2553–2562.

69 J. H. Lee, J. Cho, M. Jeon, M. Ridwan, H. S. Park, S. H. Choi, S. W. Nam, J. Han, T.-H. Lim, H. C. Ham and C. W. Yoon, *J. Mater. Chem. A*, 2016, **4**, 14141–14147.

70 J. T. Feaster, C. Shi, E. R. Cave, T. Hatsukade, D. N. Abram, K. P. Kuhl, C. Hahn, J. K. Nørskov and T. F. Jaramillo, *ACS Catal.*, 2017, **7**, 4822–4827.

71 M. Mavrikakis, B. Hammer and J. K. Nørskov, *Phys. Rev. Lett.*, 1998, **81**, 2819–2822.

72 B. Hammer and J. K. Nørskov, *Advances in Catalysis*, Academic Press, 2000, vol. 45, pp. 71–129.

This journal is © the Owner Societies 2021

Phys. Chem. Chem. Phys., 2021, **23**, 11515–11527 | 11527